Accepted Manuscript

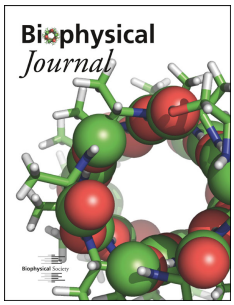

Controlling Anomalous Diffusion in Lipid Membranes

H.L.E. Coker, M.R. Cheetham, D.R. Kattnig, Y.J. Wang, S. Garcia-Manyes, M.I. Wallace

PII: S0006-3495(19)30032-3

DOI: https://doi.org/10.1016/j.bpj.2018.12.024

Reference: BPJ 9536

To appear in: *Biophysical Journal*

Received Date: 25 June 2018

Accepted Date: 14 December 2018

Please cite this article as: Coker HLE, Cheetham MR, Kattnig DR, Wang YJ, Garcia-Manyes S, Wallace MI, Controlling Anomalous Diffusion in Lipid Membranes, *Biophysical Journal* (2019), doi: https://doi.org/10.1016/j.bpj.2018.12.024.

Controlling Anomalous Diffusion in Lipid Membranes

H. L. E. Coker[1,a,b], M. R. Cheetham[1,a,b], D. R. Kattnig[c], Y. J. Wang[d], S. Garcia-Manyes[d], M. I. Wallace[a]

[a]Department of Chemistry, Britannia House, King's College London, London SE1 1DB

[b]Chemistry Research Laboratory, 12 Mansfield Road, University of Oxford, Oxford OX1 3TA

[c]Living Systems Institute & Department of Physics, University of Exeter, Stocker Road, Exeter EX4 4QD

[d]Department of Physics, Strand Building, King's College London, London WC2R 2LS

[1]Contributed equally to this work.

[*]Correspondence: mark.wallace@kcl.ac.uk

Abstract

Diffusion in cell membranes is not just simple two-dimensional Brownian motion but typically depends on the timescale of the observation. The physical origins of this anomalous sub-diffusion are unresolved, and model systems capable of quantitative and reproducible control of membrane diffusion have been recognized as a key experimental bottleneck. Here we control anomalous diffusion using supported lipids bilayers containing lipids derivatized with polyethylene glycol (PEG) headgroups. Bilayers with specific excluded area fractions are formed by control of PEG-lipid mole fraction. These bilayers exhibit a switch in diffusive behavior, becoming anomalous as bilayer continuity is disrupted. Using a combination of single-molecule fluorescence and interferometric imaging, we measure the anomalous behavior in this model over four orders of magnitude in time. Diffusion in these bilayers is well-described by a power-law dependence of the mean square displacement with observation time. Anomaleity in this system can be tailored by simply controlling the mole fraction of PEG-lipid, producing bilayers with diffusion parameters similar to those observed for anomalous diffusion in biological membranes.

Introduction

Diffusion is an essential transport mechanism in membrane biology, vital for a wide range of biological function including protein organization (1), signalling (2, 3) and cell survival (4). Interestingly, such living systems do not, in general, display the Brownian motion predicted by a simple random walk model, and instead exhibit 'anomalous' diffusion (5) where the diffusivity is dependent on the timescale of observation. This phenomenon has been reported both for three-dimensional diffusion in the cell cytosol (6) and two-dimensional diffusion in the plasma membrane (7–9).

Why and how anomalous diffusion exists in the plasma membrane has been the subject of considerable investigation (reviewed in (10)). The common underlying mechanism is thought to relate to the complex environment found in the cell membrane (11); and the presence of slower-moving obstacles (12, 13), heterogeneous diffusion (14), transient binding (15), pinning sites, and compartmentalization (11, 16, 17) have all been suggested as potential contributors to anomaleity in membrane diffusion. Here we focus on confinement, where in cellular membranes anomalous diffusion is reported in a large number of cell types (16–18) and with barrier length-scales on the order of tens to hundreds of nanometers. Overall this work has led to the adoption of a compartmentalized model of the cell membrane, where the cytoskeleton-membrane interactions impose barriers to diffusion (11, 15).

Artificial lipid bilayers have played a key role in improving our understanding of anomalous diffusion (19–24), where both phase separation (20) and protein binding (21) in supported lipid bilayers (SLBs) have been used to generate anomalous diffusion. Simulations have also been vital in advancing our understanding, with much pioneering (5, 25, 26) and recent (27–32) work in this area. In particular, simulations have helped elucidate the role of mobile and immobile obstacles in causing anomalous behavior (12, 13). Relevant to our work, simulations have also been used to better interpret single

particle tracking data (33) and provide methods to discriminate between classes of anomalous diffusion (34).

Despite these advances, discriminating between the different possible molecular mechanisms that give rise to anomalous diffusion *in vivo* remains challenging. Discrepancies between results from different techniques arise due to their different timescales of measurement, making it difficult to isolate the underlying cause of any observed anomalous diffusion. This is most clearly highlighted by Saxton et al., who published a call for 'a positive control for anomalous diffusion' as a solution to this problem (10). This positive control would be a simple and reproducible experimental model exhibiting 'readily tuneable' anomalous diffusion spanning several orders of magnitude in timescale, that would enable direct comparison of different measurement techniques.

Here we seek to address this call by engineering a simple experimental model in which it is possible to select the extent of anomalous behavior. We take advantage of previous work on the disruption of SLB formation by PEG-DPPE (35) to control nanoscale obstacle formation in a bilayer (Fig. 1A). By varying the PEG-DPPE composition in a bilayer, we expect that an increased fraction of polymer in the brush regime will result in the formation of specific defects in the bilayer, similar to interfacial or grain boundary defects caused by phases separating mixtures (36). Similar defects have also been reported using Atomic Force Microscopy (AFM) of incomplete SLB formation from small unilamellar vesicles (SUVs) (37), as well as in SLBs formed in the presence of membrane active peptides (38).

In exploiting membrane defects as a tool to help us understand anomalous diffusion we must highlight the fact these defects are *not* the cause of anomalous diffusion in cells. Despite this limitation, our simple model does allow the generation of lipid membranes with tuneable anomalous parameters relevant to the range reported in cells. Thus, we can make specific changes to the nature and size of these obstacles in order to better understand their effects on anomalous behavior, and help benchmark different experimental techniques.

The complex nanometer-scale confinement reported in cell membranes gives rise to anomalous behavior that spans from microseconds to seconds. Thus to properly characterize anomalous diffusion, it is important to apply techniques capable of studying these timescales. To access this range of timescales, we exploit a combination of two single-molecule methods: Total Internal Reflection Fluorescence (smTIRF) (39) and Interferometric Scattering (iSCAT) microscopy (40, 41). smTIRF enables the tracking of single fluorescently-labeled lipid in these membranes with super-resolved precision (Fig. 1C). Using gold nanoparticles, iSCAT enables tracking of lipid diffusion at sub-millisecond time resolutions (Fig. 1D). In combination, these techniques allow us to characterize nanoscopic diffusion using single-particle tracking that spans over four orders of magnitude in time.

Theory

Anomalous diffusion describes random molecular motion that does not display a linear scaling of the second moment with time. The most common model for anomalous diffusion is to allow the second moment to scale as a power of time (5, 42),

$$\langle \Delta r^2 \rangle = 4\Gamma \Delta t^{\alpha}, \qquad (1)$$

where α is the anomalous exponent and $\langle \Delta r^2 \rangle$ is the mean squared displacement. Here, the more familiar diffusion coefficient, *D*, is replaced by Γ, the anomalous transport coefficient. Given the form of equation 1, α can be determined from the gradient of a logarithmic plot of $\langle \Delta r^2 \rangle / 4\Delta t$ *vs.* Δt.

The transport coefficient Γ is somewhat more difficult to interpret than the anomalous exponent α, as it has dimension of $[L]^2/[T]^{\alpha}$, thus its dimensions are changing for different degrees of anomalous behavior. This apparent problem can be overcome by de-dimensionalizing the observation time (5) using a 'jump time', τ:

$$\langle \Delta r^2 \rangle = 4D\Delta t \left(\frac{\Delta t}{\tau} \right)^{\alpha - 1}. \qquad (2)$$

τ can be interpreted in terms of a length scale (λ) associated with the anomalous behavior in 2D ($\lambda = \sqrt{4D\tau}$). Combining equations 1 and 2 yields

$$\log_{10} \Gamma / D = 1 - \alpha \log_{10} \tau, \quad (3)$$

and a linear scaling of $\log_{10} \Gamma / D$ with α is expected.

Materials and Methods

Materials

1,2-dioleoyl-*sn*-glycero-3-phosphocholine (DOPC), 1,2-diphytanoyl-*sn*-glycero-3-phosphocholine (DPhPC) and 1,2-dioleoyl-*sn*-glycero-3-phosphoethanolamine-N-cap-biotinyl (biotin-DOPE) were purchased from Avanti Polar Lipids (Alabaster, AL). Texas Red 1,2-dihexadecanoyl-*sn*-glycero-3-phosphoethanol-amine (TR-DHPE) triethylammonium salt and 1,2-dipalmitoyl-*sn*-glycero-3-phosphoethanolamine-N-[methoxy(polyethylene glycol) - 1000/2000/5000] ammonium salt (PEG1/2/5K-DPPE) were purchased from Invitrogen (Eugene, OR). Goat antibiotin-conjugated 20 nm gold nanoparticles were purchased from BBI (Cardiff, UK). Standard phosphate-buffered saline (PBS) tablets (P4417), hexadecane (296317) and silicone oil AR20 (10836) were purchased from Sigma-Aldrich (St-Louis, MO). All chemicals and solvents were of analytical grade and used without further purification. 18.2 MΩ cm water (Merck Millipore, Billerica, MA) was used to prepare all solutions.

Supported Lipid Bilayers

Glass coverslips (VWR, Menzel Gläser #1) were cleaned using stepwise sonication with detergent (Decon-90), water, and propan-2-ol before being stored in water until use. Immediately before use the glass was dried under nitrogen and cleaned with oxygen plasma for 3 minutes (Diener Electronic, Femto). A well was created on each coverslip using vacuum grease (Dow Corning high vacuum grease). Lipid mixtures in chloroform (1 mg mL^{-1} 1 DOPC; 10$\times$6 mol% each TR-DHPE and biotin-DOPE) were doped with varying amounts of PEG-lipids to span a range of 0 to 10 mol%. Lipid mixtures were dried under nitrogen and placed under vacuum overnight. The dried lipids were hydrated in water and votexed before tip sonication for 15 minutes. The resulting clear, SUV suspension was centrifuged (3 minutes; 14000 g) before the supernatant was separated and retained. 50 μL of SUV stock was diluted 1:1 in buffer (PBS pH 7.4) and added to the chamber immediately. The vesicles were incubated for 60 minutes before the membranes were washed with de-gassed water and PBS.

Atomic Force Microscopy

AFM was carried out using a BioScope Resolve (Bruker, MA). An SNL-10B cantilever was used with a spring constant of 0.12 N m^{-1}. The instrument was run in peak-force tapping mode with a maximum applied force of 40 pN. Image binarization in FIJI (43) was used to determine bilayer area fraction. Auto-correlation of the images was performed in FIJI; the resultant plots were then radially-averaged before Lorentzian fitting to extract FWHMs (Fig. S3)

Fluorescence Recovery After Photobleaching

Fluorescence recovery after photobleaching (FRAP) experiments were carried out as described by Axelrod *et al.* (44) (Fig. 4b). Briefly, a DOPC SLB with 0.5 mol% TR-DHPE, was subjected to intense 532 nm laser light through a small iris for 5 s. The iris was then opened, the illumination intensity reduced, and the bilayer imaged every 5 s for the following 20 min. Fluorescence recovered in the region where the intense laser light had caused strong photobleaching. Image analysis of this recovery process yielded the diffusivity of the TR-DHPE in the SLB. This was quantified by fitting

with a modified Bessel function as outlined by Soumpasis (45). This fitting method is only applicable to bilayers exhibiting normal diffusion and as such, the bilayer containing PEG(2K)-DPPE at 2.6 mol% was not quantified.

Total Internal Reflection Fluorescence Microscopy

A 532 nm continuous-wave laser was launched into an inverted microscope (Eclipse TiE; Nikon) and focussed at the back aperture of the objective lens (60× TIRF oil-immersion NA 1.49, Nikon, $\sim$ 1.4 kW cm^{-2} at the sample) such that total internal reflection occurred. The resultant fluorescence signal was transmitted through dichroic (ZT532rdc) and bandpass (605/55) filters (both Chroma, Bellows Falls, VT) before being imaged onto an electron-multiplying CCD (iXon+ 860; Andor) at 200 Hz.

Interferometric Scattering Microscopy

A custom microscope was constructed to conduct these measurements as described (46, 47). Briefly, a 639 nm laser beam (Toptica, Graefelfing, Munich) was directed through a polarizing beam splitter and quarter wave plate (both Thorlabs, Newton, NJ) before reaching a focus at the back aperture of an objective lens (100× oil immersion NA 1.49 Nikon). Light scattered from the coverslip interface and the object of interest produce an interference pattern which is returned through the beam splitter. The resultant signal was then magnified (overall magnification 354×) and imaged onto a CMOS camera (Phantom Miro 310) where a 128 × 128 region of interest was recorded. To track gold nanoparticle (AuNP) -labelled lipids, a SLB was formed as described above and 5 μL of anti-biotin OD10 40 nm AuNP were added. After 2 hours incubation, the SLB was washed thoroughly with buffer to remove unbound nanoparticles before imaging. Image stacks of 10000 frames were recorded at 100 kHz. Image stacks were then temporally-averaged to 5 kHz to improve signal:noise for tracking.

Single-Particle Tracking

Single-particle tracking of both smTIRF and iSCAT data was performed using the TrackMate plugin for FIJI (48). Briefly, spots were detected in each frame using a Laplacian of Gaussian (LoG) filter. Tracks were then generated by linking these detected spots together using a simple linear assignment problem (LAP) tracker. The output from this was a collection of tracks containing the space-time co-ordinates of each point in the track. This data was subsequently used to obtain mean-squared displacements for different observation times, which in turn was used to obtain diffusivity values via the random walk model of diffusion. For iSCAT experiments, A median image was first subtracted from all raw images before tracking, again using TrackMate. Gaussian fitting was used to estimate the localisation precision for smTIRF (25.7 nm at 200 Hz) and iSCAT (10.3 nm at 5 kHz).

Droplet Interface Bilayers

Droplet Interface Bilayers (DIBs) were used for control experiments to create defect free bilayers to compare with our results from SLBs (Fig 5). ‘Lipid in’ DIBs were prepared following our previous protocol (49). Briefly, SUVs of DPhPC only and DPhPC + PEG(2K)-DPPE were prepared as described above and diluted with buffer to a final concentration of 0.5 mg ml^{-1}. 100 nl droplets of SUV solution were pipetted into a microfabricated tank containing hexadecane and incubated for 40 min. DPhPC (8.9 mg ml^{-1} in 9:1 hexadecane:silicone oil) was prepared from chloroform stock. A microfabricated PMMA device containing the agarose layer on a glass coverslip was incubated with the DPhPC in oil solution for 20 min. Incubated droplets were then added to the device and left for 10 min to allow bilayer formation before imaging.

Monte Carlo Simulations

To support our experimental data and help understand diffusion in this system we created a simple 2D Monte Carlo random walk in the presence of defects. For each of 200 simulated particles, two separate random walks were created (corresponding to the displacement in *x* and *y* coordinates) using a pseudorandom number generator (Mersenne Twister) with periodic boundary conditions. To mimic the defects observed in our AFM data, we defined a fixed circular obstacle of radius *R* at the centre of a square unit cell, of side *s*, shown in Figure 6A. With each step of the random walk, the new

coordinates were tested to see if they were inside an obstacle or not. If they were, then that step was rejected, and a new one generated. The resulting co-ordinates for each simulated particle were subsequently processed into tracks an analysed in an identical manner to the experimental data. These tracks represent diffusing particles that have been hindered due to the presence of obstacles, and exhibited anomalous diffusion as expected.

Results

Supported Lipid Bilayers

DOPC SLBs doped with PEG-DPPE (0 - 10 mol% PEG-DPPE; 1,2, & 5 kDa PEG) were first examined using AFM (Fig. 1B): As PEG-DPPE content increased, small defects appeared in the bilayer. Further increases in the concentration of PEG-DPPE resulted in the growth of these interfacial defects, until the system crosses the percolation threshold, leading to confined bilayer patches. Image binarization and spatial autocorrelation were used to calculate the excluded area fraction and defect length scale. The diffusive properties of these bilayers were assessed by single-particle tracking from both smTIRF and iSCAT image sequences. smTIRF was used to track individual Texas Red-labelled lipids ($\sim 10^{-6}$ mol% TR-DHPE) at 200 Hz; iSCAT tracked 40 nm antibiotin-conjugated gold nanoparticles (AuNPs) tethered to biotinylated lipids at 5 kHz.

For smTIRF, as the concentration of PEG(2K)-DPPE was increased from 0 to 5 mol%, the gradient of the $\log \langle \Delta r^2 \rangle / 4\Delta t$ *vs.* $\log \Delta t$ plot deviates from zero (Fig. 2A). Figure 2B shows the equivalent PEG(2K)-DPPE dataset arising from iSCAT. Similar plots were produced for PEG(1K)- and PEG(5K)-DPPE (Fig. S1). Gradients extracted from these plots ($\alpha - 1$) permit calculation of the anomalous exponent, α, while the y-axis intercept reports the transport coefficient, Γ. The values of α for all three PEG molecular weights are collated in Figure 2C; α transitions from 1 (free diffusion) to 0 (confined diffusion). Similary, Γ varies from free diffusion to confined as the mol% PEG-DPPE increases (Fig. 2D). These data were fit to a simple sigmoid. Both smTIRF and iSCAT measurements give rise to the same trend, and are plotted together (Figs. 2C&D, Table S1).

Binarization of our AFM data enabled us to estimate the bilayer area fraction as a function of mol% PEG-DPPE (Fig. 3A). Using this calibration, we then examined the variation in anomalous diffusion as a function of excluded area fraction. For α (Fig. 3B) and Γ (Fig. 3C), the sigmoids for the three different PEG molecular weights now overlap, showing the same trend with excluded area fraction. For α *vs.* excluded area fraction a single sigmoid fit yields a midpoint at $\alpha = 0.232 \pm 0.001$. Limiting values for Γ differ as expected between smTIRF and iSCAT experiments due to the size difference of fluorescently labelled lipids and AuNPs (50). It is also worth emphasizing that as Γ scales with α, only points with the same α values can really be compared directly.

Supported Lipid Bilayer Recovery

We sought to determine if anomalous diffusion in these bilayers is due to membrane defects. Following SPT of a bilayer with 2.6% PEG(2K)-DPPE, we performed experiments where additional DOPC SUVs were added to subsequently 'repair' the membrane. smFRET tracking of individual lipids in these experiments showed a recovery and return to normal diffusion following SUV addition (Fig. 4A). We also performed FRAP measurements on these membranes in order to measure the overall properties of the bilayer (Fig. 4B). Prior to SUV addition, recovery of fluorescence was essentially absent, with a large slow and immobile fraction. Following addition of SUVs, membranes recovered their fluorescence with a diffusion coefficient ($D = 1.75 \mu\text{m}^2\ \text{s}^{-1}$) comparable to a pure DOPC bilayer ($D = 1.81 \mu\text{m}^2\ \text{s}^{-1}$), indicative of a contiguous bilayer without confined diffusion.

Droplet Interface Bilayers

We used Droplet Interface Bilayers (DIBs) (49, 51) to create defect-free bilayers (Fig. 5A). In DIBs, defects would result in conductance across the bilayer, unstable droplets and ultimately bilayer rupture (52). DIBs with 2.6 or 5.0 mol% PEG(2K)-DPPE; $\sim 10^{-6}$ mol% TR-DHPE) were formed.

Single-particle tracking using smTIRF showed normal diffusion even for 5.0 mol% PEG-DPPE, well above the threshold value for anomalous behaviour in SLBs. Bilayers containing even 5.0 mol% PEG(2K)-DPPE exhibited normal diffusion (Fig. 5B).

Monte Carlo Simulations

To help improve our understanding of these results we constructed a Monte-Carlo simulation of anomalous diffusion where a periodic square lattice of circular, immobile obstacles of radius *R* was simulated using a unit cell with side-length *s* (Fig. 6A). A discrete-time random walk was subject to the constraint that the walk cannot enter the circular obstacle. As expected from previous similar Monte-Carlo simulations (5), anomalous behavior arises as the excluded area fraction was increased (Fig. 6B); and again a plateau of normal diffusion at short times was observed. When values were collated, a sigmoidal trend was present with $\alpha = 0$ reached at an area fraction of 0.773, near to the percolation threshold for simple fixed circular obstacles on a square lattice (0.785). Γ was best fit by a double-sigmoid (Fig. 6D, Table S1). A linear variation of $\log_{10} \Gamma / D$ with α was also reproduced from our simulation, consistent with equation 3. The characteristic length scales (λ) calculated from both simulation (Fig. 7A) and experiment (Fig. 7B) are summarized in Table S2.

Reproducing specific anomalous diffusion

To assess the usefulness of this model to produce bilayers with defined anomalous diffusion, we examined the variation of measured α with that predicted from a specific mol% PEG-DPPE (Fig. 8). From this analysis, we are able to reproduce bilayers with defined α values with a precision of 0.065 from the root mean squared deviation of target *vs.* measured values of α.

Limitations

We address directly the limitations of this model system. Confinement in cell membranes is clearly not created by membrane defects in supported bilayers, but rather is (arguably) most likely due to the excluded area created by membrane proteins and their interactions with lipids. However, despite these fundamental differences, both systems result in a similar restriction to free diffusion in the bilayer, and a parallel can be drawn between the excluded area controlled in this simple model and that inaccessible to diffusing species in cell membranes. This clearly does not exclude other potential mechanisms as the cause of anomaleity in cells, but it does provide a model system with well-defined parameters, with which to test predictions about anomalous diffusion in lipid membranes.

Theory predicts that in a system with finite hierarchy, the diffusion will return to normal behavior (with a reduced diffusion coefficient) at sufficiently long observation times (53). Figure 2A shows that over the time scales observed in these experiments, the diffusion here remains anomalous. As normal behavior returns at around 100 ms for similarly sized compartments in cells (17), our model must not possess the restricted range of compartment size that are presumably present in cell membranes. Further control of bilayer defect scaling would enable a return to normal diffusion at these timescales; for example by nano-patterning of the substrate before SLB formation (54). However, this is beyond the scope of this work.

Discussion

These experiments show the presence of PEG-DPPE can disrupt SLB formation leaving a network of defects whose area fraction is dependent on the concentration. It is bilayer continuity (not the presence of PEG-DPPE as a static obstacle) that causes this anomalous behavior. Controls (Fig. 4) confirm that normal diffusive behavior can be rescued by filling in bilayer defects, or exploiting bilayers where defects are inhibited (Fig. 5).

The variation of α and Γ with excluded area fraction shows a sigmoidal transition between free and confined diffusion. This behaviour enables us to control anomalous behaviour and select specific α values by varying the mol% of PEG-DPPE (Fig. 8), with a turning point that is itself tuneable based on PEG length (Fig. 2C). Lipid solutions in organic solvents are straightforward to produce, and our method can be used to create a model bilayer with specific α. Reported α values from both molecular

dynamics simulations (27) and measured in cell membranes (17, 55–57) span a wide range (typically 0.45 - 0.7). Using our model we can make specific and controlled changes to defect extent that encapsulate this range, providing an opportunity to use this simple model to recreate parameters that would be representative of anomalous diffusion observed *in vivo*, noting again that although the characteristics of this diffusion can be recreated, the underlying mechanism (defects in a lipid bilayer) is clearly different.

We also considered fractional moment analysis to explore if our model exhibited strong or weak self-similarity in diffusion (58) (Fig. S4), however this analysis showed strong self-similarity for all fractional moments.

By using two single-particle microscopy techniques we have sampled the anomalous behavior of this model over four orders of magnitude of time. Alone, fluorescence microscopy cannot access the divergence of the diffusivity at short times and the onset of anomalous behavior. The high frame rate of iSCAT also presents its own challenges in data management, preventing us from probing all the relevant timescales with a single technique.

Perhaps of greatest interest is the difference between plots of $\log_{10} \Gamma / D$ *vs.* α between our simulations and experiment (Fig. 7, Table S2): Only our simulation shows a variation in length scale with obstacle size. In contrast, our experimental data shows a similar gradient for all three molecular weights of PEG-DPPE. This suggests that in the experiment the size (but not number or extent) of defects produced are of a similar scale ($\sim$ 150 nm) and are independent of the PEG molecular weight. This is in agreement with our observation that the anomalous diffusion is caused by the presence of bilayer defects, as seen in our AFM data, rather than the direct presence of PEG-DPPE lipids in the bilayer. The values extracted from AFM FWHMs are smaller by around a factor of 3. There is also a modest negative correlation between FWHM and excluded area fraction (see Fig. S6).

The differences between experiment and simulation are most likely due to the different topologies for defects in the two cases: To preserve simplicity, defects in the simulation were simple circles. This is in contrast to our experimental AFM images (Fig. 2A) that show not circular, but rather interfacial defects for intermediate PEG-lipid concentrations. We therefore interpret this characteristic length scale as a descriptor of the barrier to diffusion. In our model, that is the scale associated with bilayer defects.

To help compare measurements of anomalous diffusion from different methods with different timescales Saxton proposed eight criteria with which to judge the usefulness of any ‘positive control’ for anomalous diffusion. We reproduce the conclusions here, and direct the reader to the original paper for a comprehensive discussion (10): (1) Biologically relevant length and time scales; (2) A tuneable subdiffusion exponent with a well understood mechanism, such as percolation; (3) Simple to produce; (4) The anomalous regime to extend over 2-3 orders of magnitude, and if transient anomalous subdiffusion, that normal and anomalous regimes are distinct; (5) Tracers detectable by orthogonal methods, e.g. both NMR and fluorescence; (6) Transparent; (7) Either (i) spatially homogeneous, or (ii) inhomogeneous at all length scales for a fractal substrate; (8) Stable fluorescence. Overall our system satisfies these requirements. We also were able to compare SPT results from two different experimental techniques. However, we note as our model appears anomalous at all length scales, it only satisfies one sub-case of criterion (4). Our current experiment does not have distinct normal and anomalous regimes, defined by a single specific length scale.

Conclusion

By controlling SLB formation using PEGylated lipids we are able to produce bilayers with defined anomalous diffusive properties, dependent on the excluded area fraction and the presence of bilayer defects. Thus, we hope our work in part answers the call for a simple and reproducible experimental model, readily tuneable in anomaleity over the length scales observed *in vivo*. This study also opens the way to further experiments that exclude membrane area using more complex methods than the simple inclusion of PEG-lipids presented here.

Author Contributions

HLEC, MRC, and YJW conducted the experiments. HLEC, MRC, DRK, SGM, and MIW contributed to analysis. HLEC, MRC, and MIW wrote the manuscript.

Acknowledgments

We thank the European Research Council for providing funding for this work (ERC-2012-StG-106913 CoSMiC).

References

1. Sheets, E. D., G. M. Lee, R. Simson, and K. Jacobson, 1997. Transient confinement of a glycosylphosphatidylinositol-anchored protein in the plasma membrane. *Biochemistry* 36:12449–12458.

2. Choquet, D., and A. Triller, 2003. The role of receptor diffusion in the organization of the postsynaptic membrane. *Nature Reviews Neuroscience* 4:251–265.

3. Kholodenko, B. N., 2006. Cell-signalling dynamics in time and space. *Nature Reviews Molecular Cell Biology* 7:165–176.

4. Cheema, U., Z. Rong, O. Kirresh, A. J. Macrobert, P. Vadgama, and R. A. Brown, 2012. Oxygen diffusion through collagen scaffolds at defined densities: Implications for cell survival in tissue models. *Journal of Tissue Engineering and Regenerative Medicine* 6:77–84.

5. Saxton, M. J., 1994. Anomalous diffusion due to obstacles: a Monte Carlo study. *Biophysical Journal* 66:394–401.

6. Regner, B. M., D. Vučinić, C. Domnisoru, T. M. Bartol, M. W. Hetzer, D. M. Tartakovsky, and T. J. Sejnowski, 2013. Anomalous diffusion of single particles in cytoplasm. *Biophysical Journal* 104:1652–1660.

7. Höfling, F., and T. Franosch, 2013. Anomalous transport in the crowded world of biological cells. *Reports on Progress in Physics* 76:046602.

8. Fujiwara, T. K., K. Iwasawa, Z. Kalay, T. A. Tsunoyama, Y. Watanabe, Y. M. Umemura, H. Murakoshi, K. G. N. Suzuki, Y. L. Nemoto, N. Morone, and A. Kusumi, 2016. Confined diffusion of transmembrane proteins and lipids induced by the same actin meshwork lining the plasma membrane. *Molecular Biology of the Cell* 27:1101–1119.

9. Golan, Y., and E. Sherman, 2017. Resolving mixed mechanisms of protein subdiffusion at the T cell plasma membrane. *Nature Communications* 8:15851.

10. Saxton, M. J., 2012. Wanted: A positive control for anomalous subdiffusion. *Biophysical Journal* 103:2411–2422.

11. Kusumi, A., C. Nakada, K. Ritchie, K. Murase, K. Suzuki, H. Murakoshi, R. S. Kasai, J. Kondo, and T. Fujiwara, 2005. Paradigm shift of the plasma membrane concept from the two-dimensional continuum fluid to the partitioned fluid: high-speed single-molecule tracking of membrane molecules. *Annual review of biophysics and biomolecular structure* 34:351–78.

12. Saxton, M. J., 1987. Lateral diffusion in an archipelago. The effect of mobile obstacles. *Biophysical Journal* 52:989–997.

13. Berry, H., and H. Chaté, 2014. Anomalous diffusion due to hindering by mobile obstacles undergoing Brownian motion or Orstein-Ulhenbeck processes. *Physical Review E - Statistical, Nonlinear, and Soft Matter Physics* 89:022708.

14. Manzo, C., J. A. Torreno-Pina, P. Massignan, G. J. Lapeyre, M. Lewenstein, and M. F. Garcia Parajo, 2015. Weak Ergodicity Breaking of Receptor Motion in Living Cells Stemming from Random Diffusivity. *Phys. Rev. X* 5:011021.

15. Weigel, A. V., B. Simon, M. M. Tamkun, and D. Krapf, 2011. Ergodic and nonergodic processes coexist in the plasma membrane as observed by single-molecule tracking. *Proceedings of the National Academy of Sciences* 108:6438–6443.

16. Fujiwara, T., K. Ritchie, H. Murakoshi, K. Jacobson, and A. Kusumi, 2002. Phospholipids undergo hop diffusion in compartmentalized cell membrane. *The Journal of cell biology* 157:1071–81.

17. Murase, K., T. Fujiwara, Y. Umemura, K. Suzuki, R. Iino, H. Yamashita, M. Saito, H. Murakoshi, K. Ritchie, and A. Kusumi, 2004. Ultrafine Membrane Compartments for Molecular Diffusion as Revealed by Single Molecule Techniques. *Biophysical Journal* 86:4075–4093.

18. Albrecht, D., C. M. Winterflood, M. Sadeghi, T. Tschager, F. Noé, and H. Ewers, 2016. Nanoscopic compartmentalization of membrane protein motion at the axon initial segment. *The Journal of Cell Biology* 215:37–46.

19. Schütz, G. J., H. Schindler, and T. Schmidt, 1997. Single-molecule microscopy on model membranes reveals anomalous diffusion. *Biophysical Journal* 73:1073–1080.

20. Ratto, T. V., and M. L. Longo, 2003. Anomalous subdiffusion in heterogeneous lipid bilayers. *Langmuir* 19:1788–1793.

21. Horton, M. R., F. Höfling, J. O. Rädler, and T. Franosch, 2010. Development of anomalous diffusion among crowding proteins. *Soft Matter* 6:2648.

22. Spillane, K. M., J. Ortega-Arroyo, G. de Wit, C. Eggeling, H. Ewers, M. I. Wallace, and P. Kukura, 2014. High-Speed Single-Particle Tracking of GM1 in Model Membranes Reveals Anomalous Diffusion due to Interleaflet Coupling and Molecular Pinning. *Nano letters* 14:5390–7.

23. Wu, H.-M., Y.-H. Lin, T.-C. Yen, and C.-L. Hsieh, 2016. Nanoscopic substructures of raft-mimetic liquid-ordered membrane domains revealed by high-speed single-particle tracking. *Scientific reports* 6:20542.

24. Rose, M., N. Hirmiz, J. M. Moran-Mirabal, and C. Fradin, 2015. Lipid diffusion in supported lipid bilayers: A comparison between line-scanning fluorescence correlation spectroscopy and single-particle tracking. *Membranes* 5:702–721.

25. Saxton, M. J., 1989. Lateral diffusion in an archipelago. Distance dependence of the diffusion coefficient. *Biophysical Journal* 56:615–622.

26. Saxton, M. J., 2001. Anomalous subdiffusion in fluorescence photobleaching recovery: A Monte Carlo study. *Biophysical Journal* 81:2226–2240.

27. Stachura, S., and G. R. Kneller, 2014. Anomalous lateral diffusion in lipid bilayers observed by molecular dynamics simulations with atomistic and coarse-grained force fields. *Molecular Simulation* 40:245–250.

28. Mardoukhi, Y., J.-H. Jeon, and R. Metzler, 2015. Geometry controlled anomalous diffusion in random fractal geometries: looking beyond the infinite cluster. *Phys. Chem. Chem. Phys.* 44:30134–30147.

29. Koldsø, H., T. Reddy, P. W. Fowler, A. L. Duncan, and M. S. P. Sansom, 2016. Membrane Compartmentalization Reduces the Mobility of Lipids and Proteins within a Model Plasma Membrane. *J. Phys. Chem. B* 120:8873–8881.

30. Jeon, J.-H., M. Javanainen, H. Martinez-Seara, R. Metzler, and I. Vattulainen, 2016. Protein Crowding in Lipid Bilayers Gives Rise to Non-Gaussian Anomalous Lateral Diffusion of Phospholipids and Proteins. *Physical Review X* 6:021006.

31. Bakalis, E., S. Höfinger, A. Venturini, and F. Zerbetto, 2015. Crossover of two power laws in the anomalous diffusion of a two lipid membrane. *Journal of Chemical Physics* 142:215102.

32. Javanainen, M., H. Hammaren, L. Monticelli, J.-H. Jeon, M. S. Miettinen, H. Martinez-Seara, R. Metzler, and I. Vattulainen, 2013. Anomalous and normal diffusion of proteins and lipids in crowded lipid membranes. *Faraday Discuss.* 161:397–417.

33. Kepten, E., A. Weron, G. Sikora, K. Burnecki, and Y. Garini, 2015. Guidelines for the fitting of anomalous diffusion mean square displacement graphs from single particle tracking experiments. *PLoS ONE* 10:e0117722.

34. Metzler, R., J.-H. Jeon, A. G. Cherstvy, and E. Barkai, 2014. Anomalous diffusion models and their properties: non-stationarity, non-ergodicity, and ageing at the centenary of single particle tracking. *Phys. Chem. Chem. Phys.* 16:24128–24164.

35. Kaufmann, S., G. Papastavrou, K. Kumar, M. Textor, and E. Reimhult, 2009. A detailed investigation of the formation kinetics and layer structure of poly(ethylene glycol) tether supported lipid bilayer. *Soft Matter* 5:2804.

36. Keller, D., N. B. Larsen, I. M. Møller, and O. G. Mouritsen, 2005. Decoupled phase transitions and grain-boundary melting in supported phospholipid bilayers. *Physical Review Letters* 94:025701.

37. Richter, R. P., and A. R. Brisson, 2005. Following the Formation of Supported Lipid Bilayers on Mica: A Study Combining AFM, QCM-D, and Ellipsometry. *Biophysical Journal* 88:3422–3433.

38. Oliynyk, V., U. Kaatze, and T. Heimburg, 2007. Defect formation of lytic peptides in lipid membranes and their influence on the thermodynamic properties of the pore environment. *Biochimica et Biophysica Acta - Biomembranes* 1768:236–245.

39. Axelrod, D., T. Burghardt, and N. Thompson, 1984. Total internal reflection fluorescence. *Annual Review of Biophysics* 13:247–268.

40. Lindfors, K., T. Kalkbrenner, P. Stoller, and V. Sandoghdar, 2004. Detection and Spectroscopy of Gold Nanoparticles Using Supercontinuum White Light Confocal Microscopy. *Physical Review Letters* 93:037401.

41. Ortega-Arroyo, J., and P. Kukura, 2012. Interferometric scattering microscopy (iSCAT): new frontiers in ultrafast and ultrasensitive optical microscopy. *Physical chemistry chemical physics : PCCP* 14:15625–36.

42. Havlin, S., and D. Ben-Avraham, 2002. Diffusion in disordered media. *Advances in Physics* 51:187–292.

43. Schindelin, J., I. Arganda-Carreras, E. Frise, V. Kaynig, M. Longair, T. Pietzsch, S. Preibisch, C. Rueden, S. Saalfeld, B. Schmid, J.-Y. Tinevez, D. J. White, V. Hartenstein, K. Eliceiri, P. Tomancak, and A. Cardona, 2012. Fiji: an open-source platform for biological-image analysis. *Nature Methods* 9:676–682.

44. Axelrod, D., D. E. Koppel, J. Schlessinger, E. Elson, and W. W. Webb, 1976. Mobility measurement by analysis of fluorescence photobleaching recovery kinetics. *Biophysical Journal* 16:1055–1069.

45. Soumpasis, D. M., 1983. Theoretical analysis of fluorescence photobleaching recovery experiments. *Biophysical Journal* 41:95–97.

46. Kukura, P., H. Ewers, C. Müller, A. Renn, A. Helenius, and V. Sandoghdar, 2009. High-speed nanoscopic tracking of the position and orientation of a single virus. *Nature methods* 6:923–7.

47. Ortega Arroyo, J., D. Cole, and P. Kukura, 2016. Interferometric scattering microscopy and its combination with single-molecule fluorescence imaging. *Nature protocols* 11:617–33.

48. Tinevez, J. Y., N. Perry, J. Schindelin, G. M. Hoopes, G. D. Reynolds, E. Laplantine, S. Y. Bednarek, S. L. Shorte, and K. W. Eliceiri, 2017. TrackMate: An open and extensible platform for single-particle tracking. *Methods* 115:80–90.

49. Leptihn, S., O. K. Castell, B. Cronin, E.-H. Lee, L. C. M. Gross, D. P. Marshall, J. R. Thompson, M. Holden, and M. I. Wallace, 2013. Constructing droplet interface bilayers from the contact of aqueous droplets in oil. *Nature protocols* 8:1048–57.

50. Mascalchi, P., E. Haanappel, K. Carayon, S. Mazères, and L. Salomé, 2012. Probing the influence of the particle in Single Particle Tracking measurements of lipid diffusion. *Soft Matter* 8:4462.

51. Bayley, H., B. Cronin, A. Heron, M. a. Holden, W. L. Hwang, R. Syeda, J. Thompson, and M. Wallace, 2008. Droplet interface bilayers. *Molecular bioSystems* 4:1191–208.

52. Sengel, J. T., and M. I. Wallace, 2016. Imaging the dynamics of individual electropores. *Proceedings of the National Academy of Sciences* 113:5281–5286.

53. Saxton, M. J., 2007. A biological interpretation of transient anomalous subdiffusion. I. Qualitative model. *Biophysical journal* 92:1178–91.

54. Tsai, J., E. Sun, Y. Gao, J. C. Hone, and L. C. Kam, 2008. Non-Brownian diffusion of membrane molecules in nanopatterned supported lipid bilayers. *Nano Letters* 8:425–430.

55. Schwille, P., J. Korlach, and W. W. Webb, 1999. Fluorescence correlation spectroscopy with single-molecule sensitivity on cell and model membranes. *Cytometry* 36:176–182.

56. Feder, T. J., I. Brust-Mascher, J. P. Slattery, B. Baird, and W. W. Webb, 1996. Constrained diffusion or immobile fraction on cell surfaces: A new interpretation. *Biophysical Journal* 70:2767–2773.

57. Smith, P. R., I. E. Morrison, K. M. Wilson, N. Fernández, and R. J. Cherry, 1999. Anomalous diffusion of major histocompatibility complex class I molecules on HeLa cells determined by single particle tracking. *Biophysical Journal* 76:3331–3344.

58. Ferrari, R., A. Manfroi, and W. Young, 2001. Strongly and weakly self-similar diffusion. *Physica D: Nonlinear Phenomena* 154:111–137.

Supplementary Material

An online supplement to this article can be found by visiting BJ Online at `http://www.biophysj.org`.

Figure 1: **Experimental scheme and raw data**. (**A**) Cartoon of supported lipid bilayer formation. Fusion of small unilamellar vesicles containing PEGylated lipids creates supported lipid bilayers on glass. As the mole fraction of PEGylated lipids increases (left - low, right - high), defects form in the bilayer that that act as obstacles, generating anomalous diffusion. (**B**) AFM shows an increase in defect area fraction with increasing mol% PEG-(2K)DPPE (scale 500 nm). (**C&D**)Representative single-particle tracking of smTIRF (**C**) and iSCAT **D**) images (scale 10 μm and 1 μm, respectively).

Note iSCAT and smTIRF experiments require different magnifications, hence different image sizes and thus scale bars. Example extracted particle tracks are shown in orange.

Figure 2: **Variation in SLB anomalous diffusion with mol% PEG-DPPE.** Logarithmic plots of $\langle \Delta r^2 \rangle / 4\Delta t$ *vs.* Δt have a gradient corresponding to the anomalous exponent, α. (**A**) For smTIRF anomalous sub-diffusion increased as the mol% PEG(2K)-DPPE was increased from 0 (black) to 5 (yellow). (**B**) A similar variation of α using iSCAT to access shorter timescales was observed for 0 (black) to 2.6 (red) mol% PEG(2K)-DPPE. (**C&D**) Variation of α and Γ with mol% PEG-DPPE. PEG(1K)- (blue triangles), PEG(2K)- (red circles) and PEG(5K)-DPPE (green squares) including both smTIRF (open markers, solid fit lines) and iSCAT data (closed markers, dashed fit lines). Error bars (grey) throughout represent standard errors. Fig. S1 provides expanded legends for these plots.

Figure 3: **Variation in SLB anomalous diffusion with excluded area fraction.** Image auto-thresholding (see Methods) was used to determine the excluded area fraction from AFM images. Sigmoid fitting of excluded area fraction *vs.* mol% PEG-DPPE provides a calibration curve to convert mol% PEG-DPPE data in Fig. 2 to excluded area fraction; for PEG(1K)- (blue triangles), PEG(2K)- (red circles) and PEG(5K)-DPPE (green squares). Variation of α (**B**) and Γ (**C**) with excluded area fractions including both smTRIF (open markers, solid fit lines) and iSCAT data (closed markers, dashed fit lines). Error bars (grey) throughout represent standard errors.

Figure 4: **Bilayer patches cause anomalous behaviour.** (**A**) A SLB exhibiting anomalous behaviour (DOPC; 2.6% PEG(2K)-DPPE, red) was incubated with DOPC SUVs. SUVs ruptured within the defects repaired the bilayer and returned normal diffusion (grey). (**B**) FRAP shows similar behaviour, with 2.6% PEG(2K)-DPPE bilayers exhibiting a large slow and immobile fraction (red). Upon addition of DOPC SUVs, diffusion again recovers ($D = 1.75\,\mu\mathrm{m}^2\ \mathrm{s}^{-1}$, mobile fraction 0.99, grey)) to values comparable to a pure DOPC bilayer ($D = 1.81\,\mu\mathrm{m}^2\ \mathrm{s}^{-1}$, mobile fraction 1.00, black).

Figure 5: **Defect-free membranes show normal diffusion.** DIBs were used to create unsupported lipid bilayers and confirm PEG-lipids alone do not result in anomalous behaviour. (**A**) Cartoon of DIB experiment. (**B**) DOPC DIBs containing PEG-DPPE and $\sim 10^{-6}$ mol% TR-DHPE) were generated. Here, single-particle tracking using smTIRF showed normal diffusion for 0 (black), 2.6 (red) and 5.0 (yellow) mol% PEG(2K)-DPPE.

Figure 6: **Monte Carlo simulations of anomalous diffusion**. (**A**) Schematic of the unit cell. (**B**) Diffusion analysis of the resultant tracks showed similar behavior to experiment ($R = 500$ nm, $D = 3\,\mu\mathrm{m}^2\ \mathrm{s}^{-1}$). (**C&D**) A similar trend to experiment was also present for α and Γ for $R =$ 150 nm, 500 nm and 1 μm (grey triangles, black circles, teal squares respectively).

Figure 7: **Anomalous scaling supports as expected from** 3**.** (**A**) Plots of $\log_{10}\ \Gamma / D$ *vs.*α show the expected linear relation, dependent on obstacle size; shown for $R =$ 150 nm, 500 nm and 1 μm (grey triangles, black circles, teal squares respectively). (**B**) Similar plots for our experimental data show an essentially static linear relationship for different PEG lengths. PEG(1K)- (blue triangles), PEG(2K)- (red circles) and PEG(5K)- (green squares).

Figure 8: **Measured** *vs.* **target** α**.** PEG-DPPE mole fractions were determined from target α values, predicted using our sigmoid fit of α*vs.* mol% PEG-DPPE (Fig. 2C). Analysis of SPT from these bilayers then returned our experimentally-measured α. Data is shown for PEG1K (blue triangles), PEG2K (red circles), and PEG5K (green squares). The root mean squared standard deviation between measured and target α was 0.065.

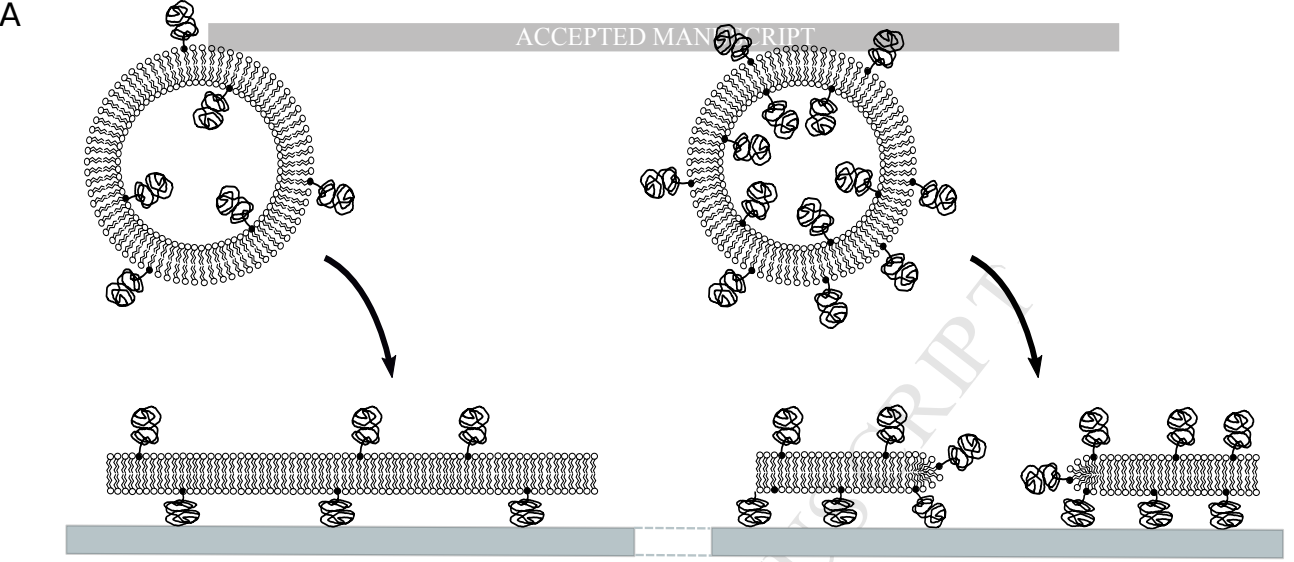

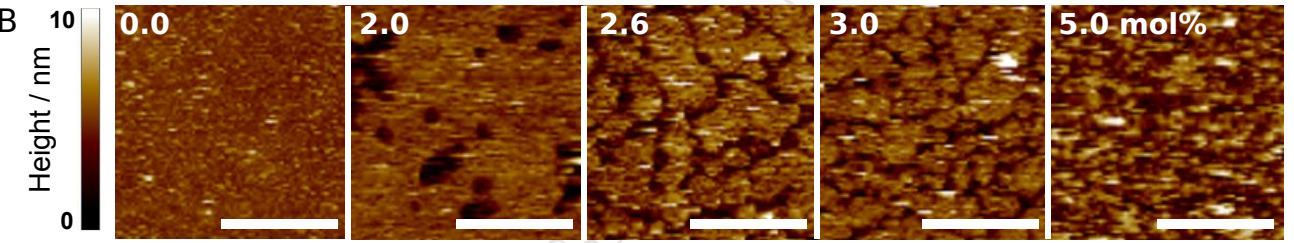

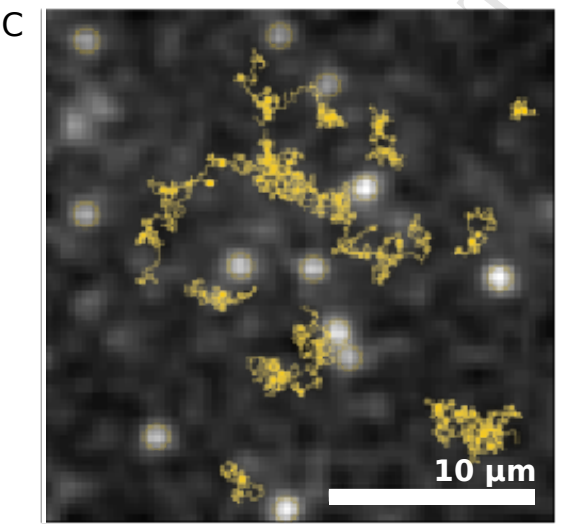

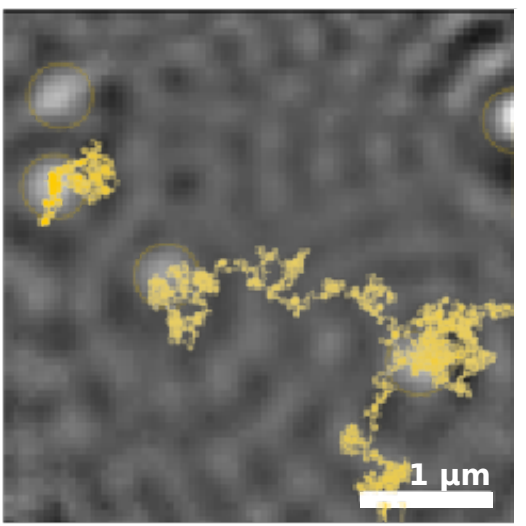

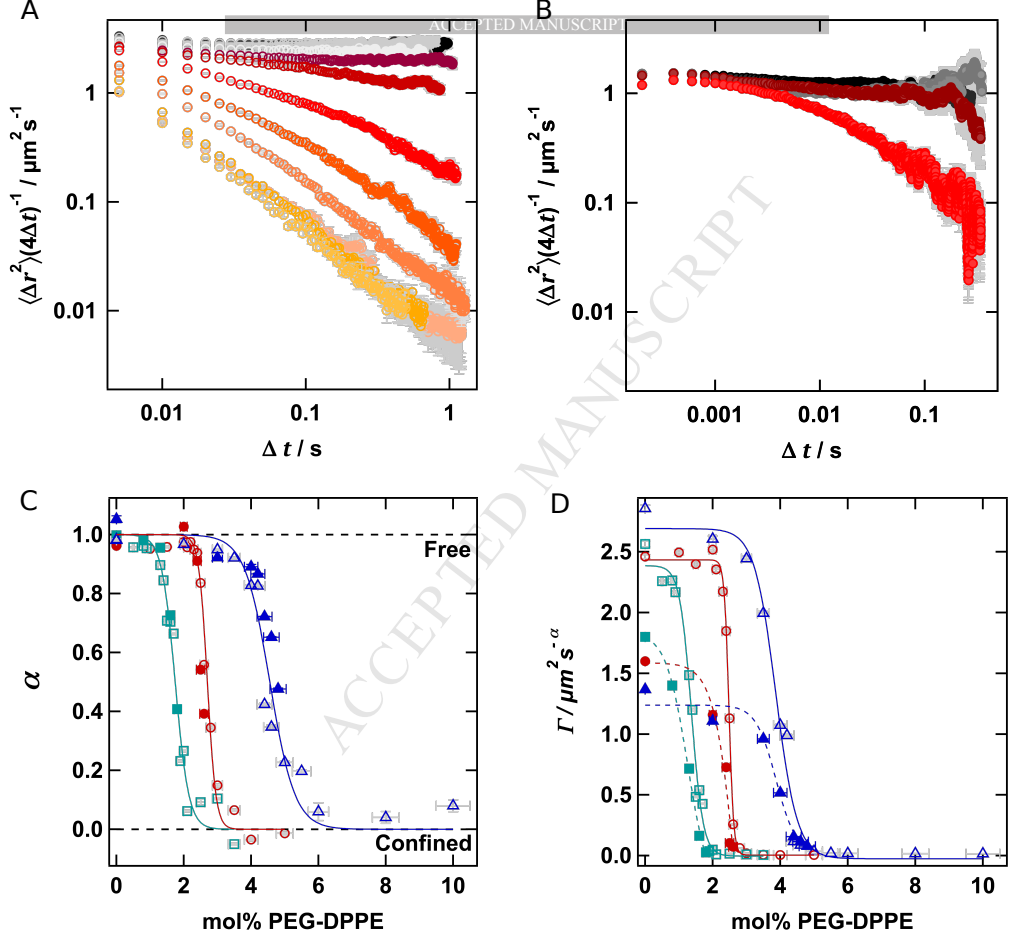

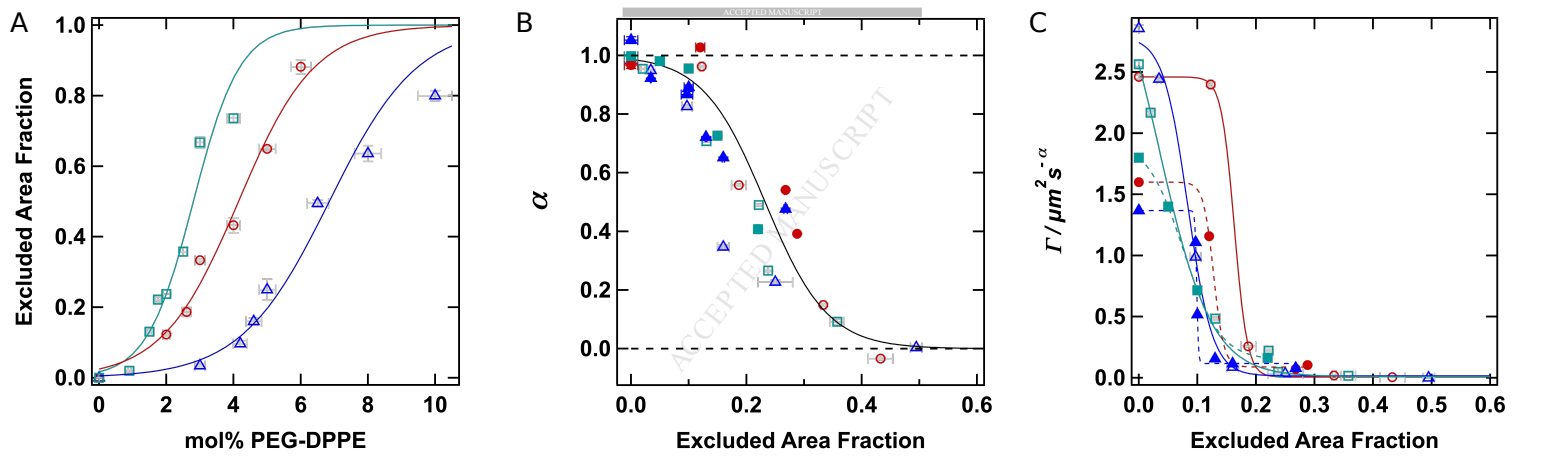
A
Excluded Area Fraction
mol% PEG-DPPE
B
α
Excluded Area Fraction
C
Γ / μm² s^-α
Excluded Area Fraction

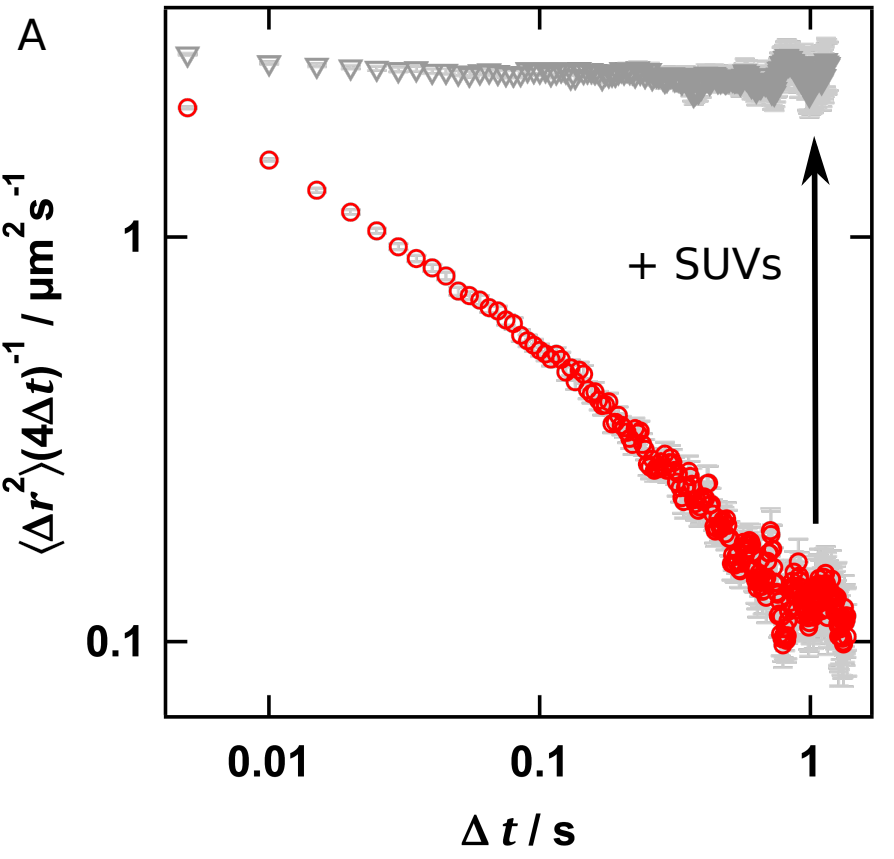
A
1
0.1
+ SUVs
0.01
0.1
1
Δ t / s

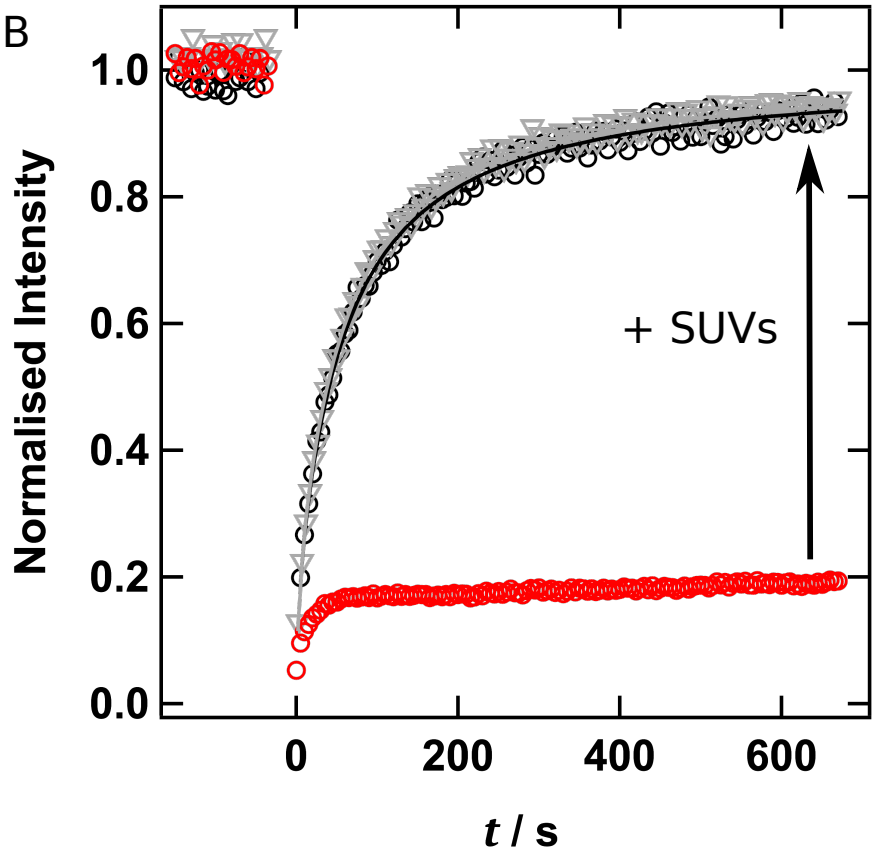
B
Normalised Intensity
1.0
0.8
0.6
0.4
0.2
0.0
+ SUVs
0
200
400
600
t / s

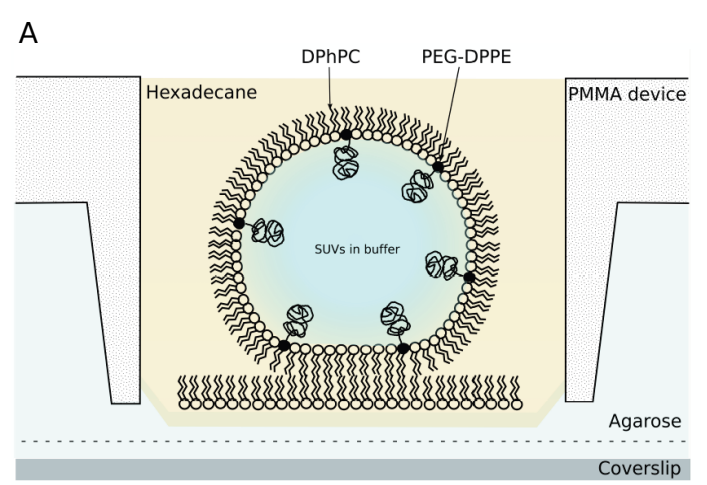
A
DPhPC
PEG-DPPE
Hexadecane
PMMA device
SUVs in buffer
Agarose
Coverslip

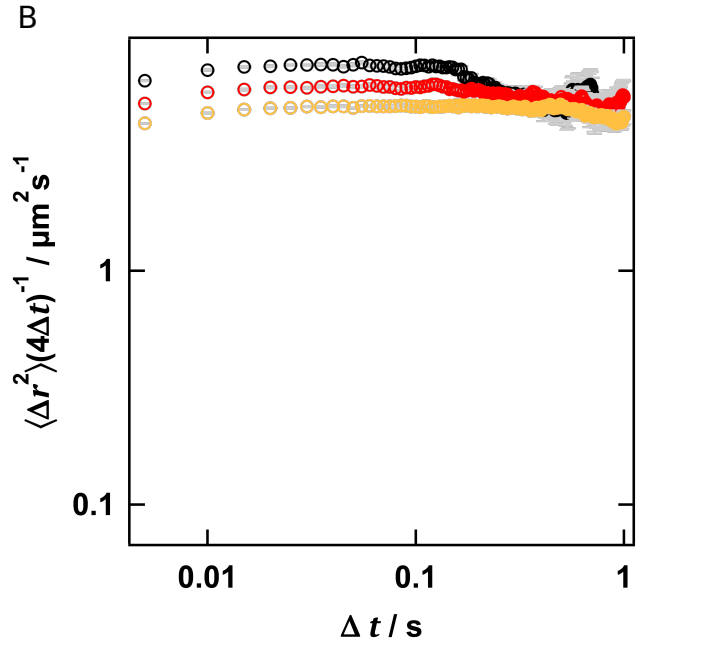
B
$\langle \Delta r^2 \rangle (4\Delta t)^{-1}$ / μm^2 s^{-1}
1
0.1
0.01
0.1
1
Δ t / s

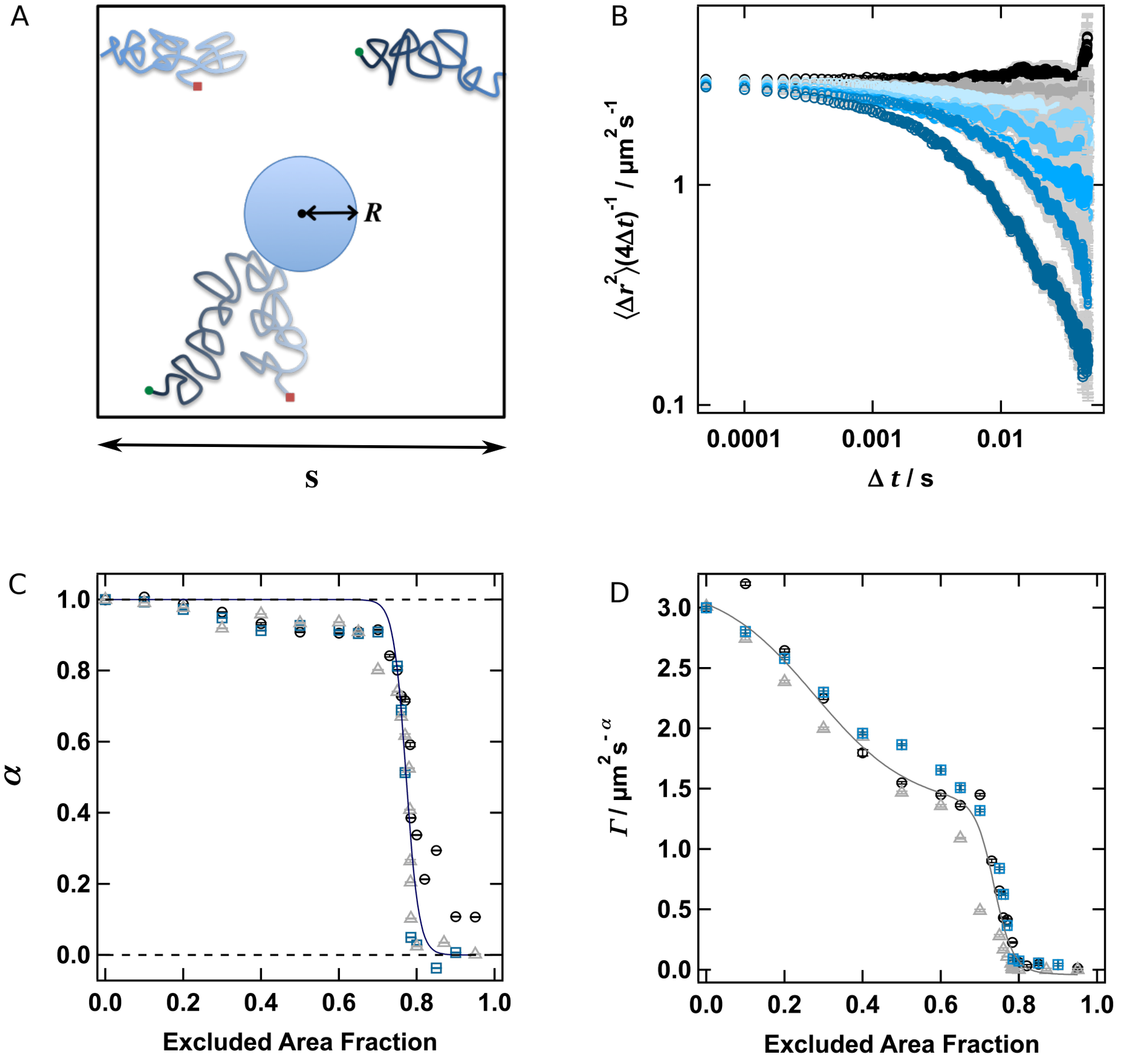
A
R
S
B
$\langle \Delta r^2 \rangle (4\Delta t)^{-1}$ / μm^{2}s^{-1}
1
0.1
0.0001
0.001
0.01
Δ t / s
C
α
1.0
0.8
0.6
0.4
0.2
0.0
0.0
0.2
0.4
0.6
0.8
1.0
Excluded Area Fraction
D
Γ / μm^{2}s$^{-\alpha}$
3.0
2.5
2.0
1.5
1.0
0.5
0.0
0.0
0.2
0.4
0.6
0.8
1.0
Excluded Area Fraction

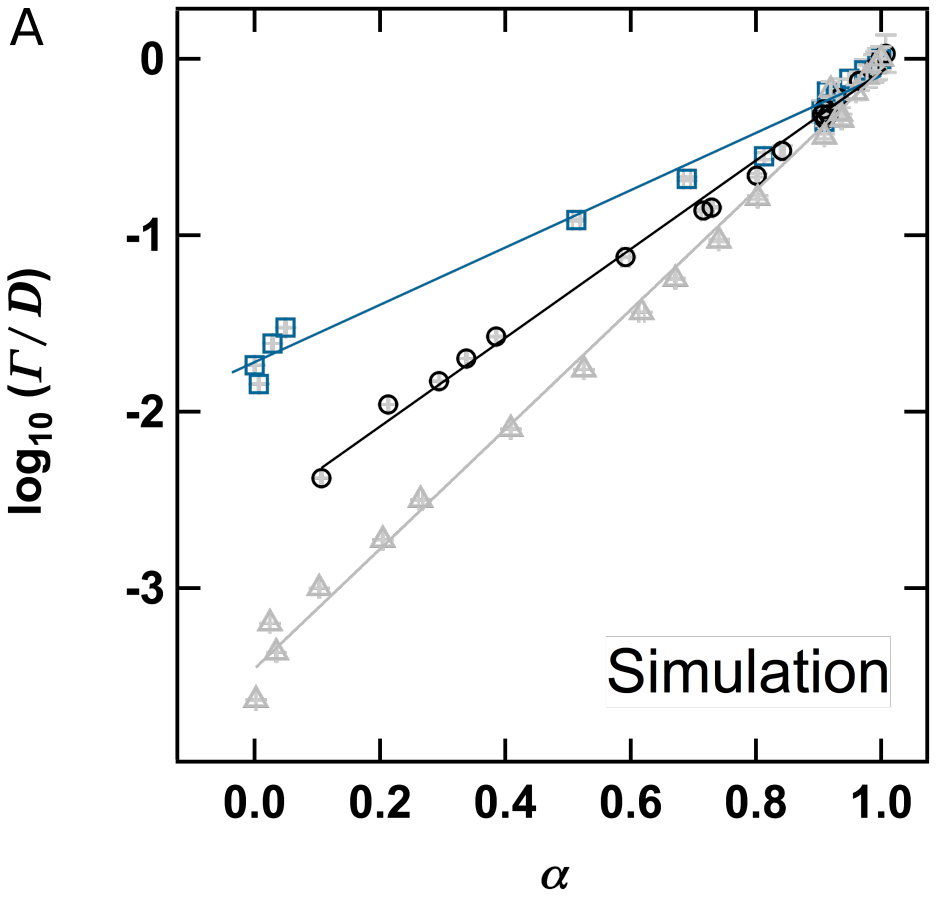
A
0
-1
-2
-3
$\log_{10}(\Gamma/D)$
Simulation
0.0
0.2
0.4
0.6
0.8
1.0
α

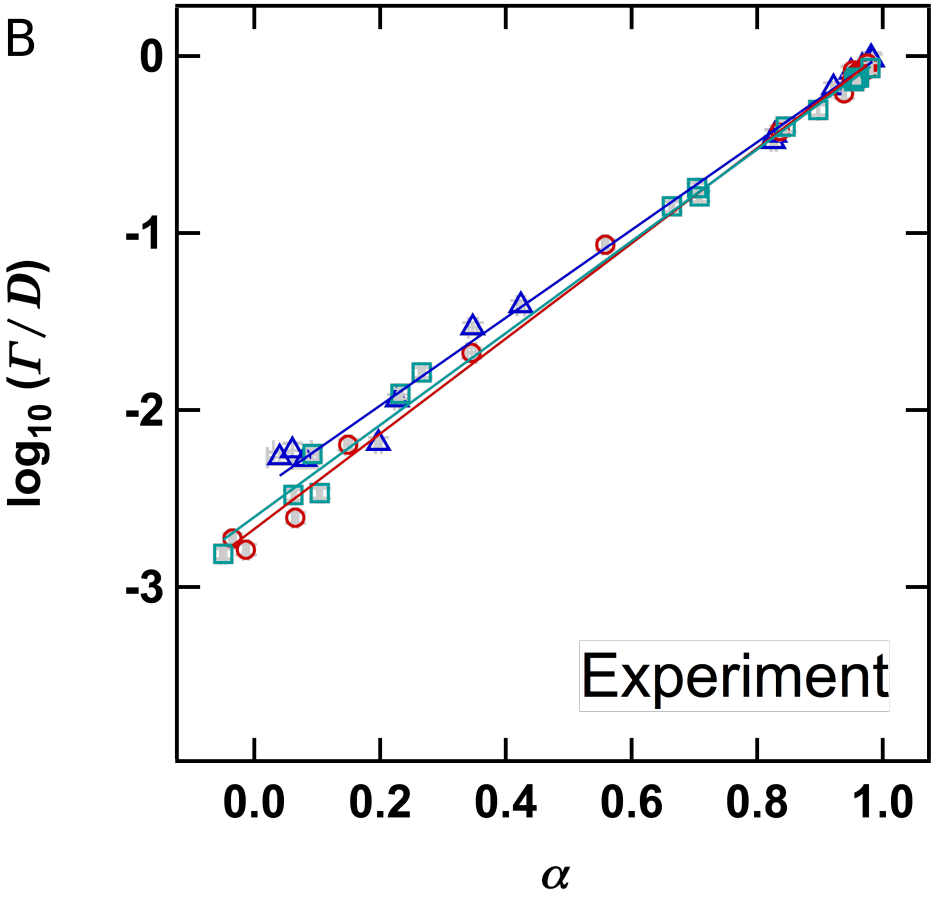
B
0
-1
-2
-3
$\log_{10}(\Gamma/D)$
Experiment
0.0
0.2
0.4
0.6
0.8
1.0
α